Temporal Localized Turing Patterns in Mode-Locked Semiconductor Lasers

Adrian Bartolo, Nathan Vigne, Mathias Marconi, Grégoire Beaudoin, Konstantinos Pantzas, Isabelle Sagnes, Guillaume Huyet, Fabian Maucher, Svetlana Gurevich, Julien Javaloyes, et al.

▶ **To cite this version:**

Adrian Bartolo, Nathan Vigne, Mathias Marconi, Grégoire Beaudoin, Konstantinos Pantzas, et al.. Temporal Localized Turing Patterns in Mode-Locked Semiconductor Lasers. Optica, 2022, 10.1364/OPTICA.471006 . hal-03858926

HAL Id: hal-03858926

https://hal.science/hal-03858926

Submitted on 17 Nov 2022

Temporal Localized Turing Patterns in Mode-Locked Semiconductor Lasers

Adrian Bartolo
Université Côte d'Azur
Nathan Vigne
Institut d'Electronique et des Systèmes
Mathias Marconi
Université Côte d'Azur
Grégoire Beaudoin
CNRS
Konstantinos Pantzas
Centre de Nanosciences et de Nanotechnologies https://orcid.org/0000-0002-2297-3247
Isabelle Sagnes
Centre de Nanosciences et de Nanotechnologies, C2N UMR 9001, CNRS, Université Paris Sud, Université Paris Saclay, 91120 Palaiseau, France https://orcid.org/0000-0001-8068-6599
Guillaume Huyet
Université Côte d'Azur
Fabian Maucher
Universitat de les Illes Baleares
Svetlana Gurevich
University of Münster
Julien Javaloyes
Departament de Física, Universitat de les illes Baleares https://orcid.org/0000-0001-9131-4483
Arnaud Garnache
Institut d'Electronique et des Systèmes
Massimo Giudici (massimo.giudici@inphyni.cnrs.fr)
Université Côte d'Azur https://orcid.org/0000-0002-7600-4927

Research Article

Keywords: dissipative solitons, pattern formation, mode-locking

Posted Date: August 5th, 2022

DOI: https://doi.org/10.21203/rs.3.rs-1846582/v3

Temporal Localized Turing Patterns in Mode-locked Semiconductor Lasers

A. BARTOLO,[1] N. VIGNE,[2], M. MARCONI,[1] G. BEAUDOIN,[3] K. PANTZAS,[3] I. SAGNES,[3] G. HUYET,[1] F. MAUCHER,[4] S. GUREVICH,[5] J. JAVALOYES,[4] A. GARNACHE,[2] AND M. GIUDICI[1,*]

[1] Université Côte d'Azur, CNRS, Institut de Physique de Nice, 06560 Valbonne, France
[2] Institut d'Electronique et des Systèmes, CNRS UMR5214, 34000 Montpellier, France
[3] Centre de Nanosciences et de Nanotechnologies, CNRS UMR 9001, Université Paris-Saclay, 91120 Palaiseau, France
[4] Departament de Física, Universitat de les Illes Baleares, C/Valldemossa km 7.5, 07122 Mallorca, Spain
[5] Institute for Theoretical Physics, University of Münster, Wilhelm-Klemm-Str. 9, 48149 Münster, Germany
[*] massimo.giudici@inphyni.cnrs.fr

Abstract: We show that large aspect-ratio Vertical External-Cavity Surface-Emitting Lasers (VECSELs) with a saturable absorber can be operated in the regime of spatio-temporal mode-locking. The emitted pulses exhibit a spatial profile resulting from the phase locking between an axial plane-wave with a set of tilted waves having a hexagonal arrangement in the Fourier space. We show that these pulsating patterns are temporally localized, i.e. they can be individually addressed by modulating the optical pump.The theoretical analysis shows that the emergence of these pulsating patterns is a signature of a Turing instability whose critical wave vector depends on spherical aberrations of the optical elements. Our result reveals that large aspect-ratio VECSELs offer unique opportunities for studying fully developed spatio-temporal dynamics.

1. Introduction

Large aspect-ratio (Large Fresnel number) lasers [1, 2] are a playground for studying pattern formation ruled by paradigmatic partial differential equations [3–8]. A variety of dissipative structures have been experimentally reported as the result of self-organization, including phase singularities [9, 10], Turing instabilities [11] and, in bistable laser cavities, Localized Structures (LSs) [12–16]. The latter, in particular, have attracted a lot of attention in the last thirty years for their application to information processing [17]. LSs in optical resonators [18–21], often called Cavity Solitons, are narrow beams of light appearing in the transverse section of a resonator that can be individually switched on and off by a local perturbation [22].

More recently, the concept of LSs has been extended to the time domain: temporal LSs are individually addressable pulses traveling back and forth inside the cavity [23–26]. In semiconductor lasers, temporal LSs have been implemented within the regime of passive mode-locking (PML) induced by a saturable absorber [27–30]. It has been shown that, if the cavity round-trip τ is larger than the gain recovery τ_g and above a critical modulation depth of the saturable absorber, a variety of mode-locked states with a different number of pulses per round trip coexist with the off solution. In these conditions, mode-locked pulses become localized and they can be individually addressed.

Temporal LS have been so far implemented in laser cavities emitting on a single-transverse mode operation. However, it was recently shown that passively mode-locked Vertical External-Cavity Surface-Emitting Lasers (VECSEL) are promising candidates for fulfilling both the large aspect ratio condition and the requirements for temporal LSs [31]. A VECSEL featuring these properties would be a laser platform ideally suited for the analysis of fully developed spatio-temporal dynamics. These complex phenomena are attracting an increasing interest in the last years [32, 33], in particular after the observation of spatio-temporal mode-locking in multimode optical fibers [34, 35]. An overview of the applications of multimode photonics, where light is structured both in time and space, has recently appeared [36].

In this paper we realize a spatio-temporal mode-locked VECSEL and we operate it in the regime of temporal LS. The mode-locked pulses exhibit a spatial profile consisting of a combination of an axial plane-wave with a set of tilted waves having a hexagonal arrangement in the Fourier space. These plane waves are phase locked and their interference gives birth to an hexagonal pattern in the near-field emission profile. We show that these spatio-temporal mode-locked pulses can be individually addressed by shining short pump pulses, hence we call them temporal localized patterns. Our theoretical analysis reveals that they arise from a Turing instability whose critical wave vector is determined by spherical aberrations of the optical elements.

2. Experimental Set-up

In this paper we design, realize and operate a PML VECSEL fulfilling large aspect-ratio condition and, at the same time, hosting temporal LSs. While the former requires a broad-area pumped region and nearly self-imaging (SI) external cavity [13, 14, 37], temporal LSs appear from PML when the external cavity roundtrip is larger than the gain recombination time ($\tau > \tau_g$) and when modulation depth of the saturable absorber is above a critical value [27, 31, 38]. Accordingly, we consider an L-shaped VECSEL delimited by the gain mirror (also called 1/2 VCSEL) and by a semiconductor saturable absorber mirror (SESAM) (see Fig. 1). The gain mirror is optically pumped at 808 nm by a flat-top elliptical profile having an horizontal axis of 90 μm and a vertical one of 50 μm (see Supplemental 1-3). Light extraction occurs through a high reflective beam splitter (>99.5% reflectivity) which reflects the intracavity radiation. This L-shape geometry avoids the anisotropies that would have been introduced by using a transmitting splitter in a linear cavity. The output beam from the VECSEL is sent to the detection part where the far-field and near-field profiles are imaged on two CCD cameras. The near-field is also imaged on an array of optical fibers for spatially resolved detection at 10 GHz bandwidth. Finally, the total emission is monitored by a 33 GHz bandwidth detection system and by an optical spectrum analyzer.

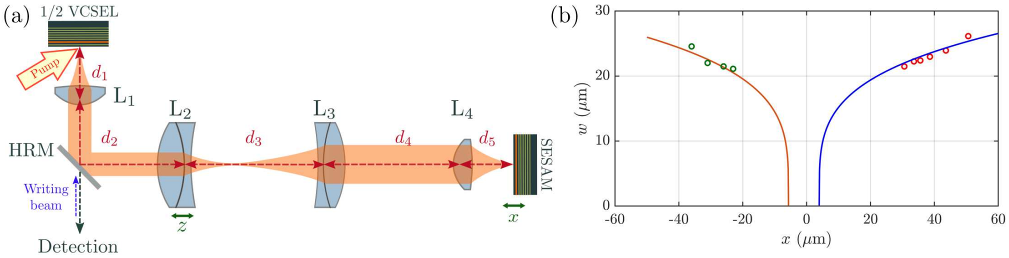

Fig. 1. a) Experimental set-up showing the L-shape VECSEL. d_1: distance between the gain section and lens L_1, d_2: distance between L_1 and lens L_2, d_3: distance between L_2 and lens L_3, d_4: distance between $L_3$and lens L_4, d_5: distance between L_4 and the SESAM, HRM= high reflectivity beam splitter (>99.5% at 1.060 nm). b) Calculated waist size of the fundamental Gaussian mode on the gain mirror (see Supplemental 1-2B, Eq. S5) as a function of the position of the SESAM ($x = d_5 - f_c$) for f_{th}=40 mm and for two positions of z : $z = 2.5$ mm (blue curve) and $z = -3.5$ mm (red curve). For $f_{th} = 40$ mm, SI condition condition is given by: $z_0 = -0.8$ mm, $x_0 = -1.3$ μm, hence, in terms of $\Delta z = z - z_0$, $\Delta z = +3.3$ mm (blue curve) and $\Delta z = -2.7$ mm (red curve). These numerical curves fit with good agreement the experimentally measured values of w when the VECSEL is pumped at 230 mW. At this power thermal lens exhibits a focal length of $f_{th} \approx 40$mm [39].

2.1. Design of the element of the VECSEL

The gain mirror is based on a GaAs substrate with 12 strain-balanced InGaAs/GaAsP quantum wells (QWs) designed for barrier optical pumping and emitting at $1.06\,\mu$m. It has been designed for standing the high level of losses in SI external cavity (see Supplemental 1-1). The SESAM features a single strained InGaAs/GaAs QW located near the external surface [40] leading to recombination rate approximately two orders of magnitudes faster than the gain medium. It has been engineered for achieving a modulation depth larger than 8 % between the saturated regime and the unsaturated one (saturable losses) for obtaining bistability of the VECSEL close to threshold [31]. Moreover, the amount of saturable losses experienced by the electromagnetic field inside the cavity is varied by tuning the gain mirror and the SESAM microcavities resonances (λ_G and λ_{SA} respectively, $\delta\lambda = \lambda_{SA} - \lambda_G$), as detailed in Supplemental 1-1

2.2. Design of the external cavity and SI condition

VECSEL external cavity (see Fig. 1a)) has been designed to fulfill the requirement $\tau > \tau_g \sim 1ns$ and SI condition after one roundtrip. In addition, the SESAM and gain mirror need to be placed in conjugate planes with a magnification factor M larger than one for saturating efficiently the SESAM.

Accordingly we use a four-lenses arrangement where the first lens (L1, the one closest to the gain section) and the last lens (L4, the one closest to the SESAM) are large numerical aperture aspheric collimators ($f_1 = f_4 = f_c$ =8 mm) and L2 and L3 are achromatic lenses having f_2 = 100mm and f_3 =200 mm. In the cold cavity situation, SI condition can be achieved through a telecentric arrangement of these optical elements, i.e. lenses are placed at distances given by the sum of their focal lengths (d_1=f_1, d_2=f_1+f_2, d_3=f_2+f_3, d_4=f_3+f_4, d_5=f_4), thus making a total cavity length L=632 mm (cavity round-trip time $\tau \approx 4.2\,$ns). In terms of ray transfer matrix from the gain section to the SESAM, this telecentric arrangement is described by the ABCD matrix

$$\begin{pmatrix} A & B \\ C & D \end{pmatrix} = \begin{pmatrix} 1/M & 0 \\ 0 & M \end{pmatrix} \tag{1}$$

where $M = f_3/f_2 = 2$, while the roundtrip transfer matrix gives the identity matrix, as required by SI condition.

However, the presence of a pump induced lens onto the gain section modifies strongly the positions of lenses for achieving SI condition with respect to the cold cavity situation, as shown in Supplemental 1-2A. This pump induced lens has a focal length f_{th} spanning from 10 to 80 mm depending on the pump level [39] (Supplemental 1-3). SI condition can be restored only by modifying the position of (at least) two lenses around their telecentric position and we choose to adjust micrometrically the position of the SESAM and the position of L_2. By calling x the offset of d_5 with respect to telecentric position ($x = d_5 - f_c$) and z the offset of d_2 with respect to telecentric position ($z = d_2 - (f_c + f_2)$), the SI condition in presence of the pump induced lens is: $z_0(f_{th}) = -\frac{f_c^2}{2f_{th}}$ and $x_0(f_{th}) = -\frac{f_c^4}{2M^2 f_2^2 f_{th}}$. (see Supplemental 1-2A for full calculations). For focal lengths values in our experiment, one finds that z_0 is of the order of few millimeters, while x_0 will be of the order of few microns since $f_2 >> f_c$. Hence, by adjusting z and x it is possible to achieve SI condition for any value of f_{th}.

From the experimental point of view, the precision requirement on the positions of the optical elements make unrealistic to achieve SI condition by placing these elements at the calculated positions. ABCD transfer matrix from the gain section to the SESAM in presence of deviations from SI condition $\Delta x = x - x_0$ and $\Delta z = z - z_0$ reads:

$$\begin{pmatrix} A & B \\ C & D \end{pmatrix} = \begin{pmatrix} 1/M + \frac{(\Delta z)^2}{M^2 f_2^2} - \frac{\Delta x \Delta z}{f_c^2} & M\Delta x - \frac{f_c^2 \Delta z}{f_2^2 M} \\ -M\frac{\Delta z}{f_c^2} & M \end{pmatrix} \tag{2}$$

The coefficients of the matrix defined in Eq. (2) can be used to calculate the stability of the cavity and the waist w of the fundamental Gaussian beam on the gain mirror as a function of x and z around SI condition positions, as detailed in Supplemental 1-2B

Close to SI condition, stability of the cavity requires $\Delta x > 0$ when $\Delta z > 0$ and $\Delta x < 0$ when $\Delta z < 0$, while the analysis of w is shown in Fig. 1 b). We can notice that the waist of the fundamental Gaussian as a function of the position of the SESAM $w(x)$ exhibits an opposite behavior depending on whether $\Delta z > 0$ or $\Delta z < 0$. For negative values of Δz (red curve in Fig. 1 b)), w increases when approaching the SESAM to L_4. For $\Delta z > 0$ (blue curve in Fig. 1b)) w increases with the distance between the SESAM and L_4. This behavior is clearly observed in the experiment and it enables an accurate observational assessment of the SI condition.

Finally, it is worth noting that, close to SI condition, the ABCD roundtrip matrix can be approximated to (see Supplemental 1-2C)

$$\begin{pmatrix} A_{RT} & B_{RT} \\ C_{RT} & D_{RT} \end{pmatrix} = \begin{pmatrix} 1 & 2(M^2\Delta x) \\ -2\frac{\Delta z}{f_c^2} & 1 \end{pmatrix} \tag{3}$$

3. Experimental Results

As shown in Fig. 1 b), the analysis of $w(x)$ from Eq. (2) together with experimental measurements of $w(x)$ allow to determine the cavity parameters with rspect to SI condition. As $\mid \Delta x \mid \rightarrow 0$ the waist of the fundamental Gaussian decreases and, when $\mid w \mid < 20\ \mu$m, spatially extended patterns appear to match the broad pumped section. In Fig. 2 we show the time-averaged spatial profile of a typical pattern observed when $\Delta x \rightarrow 0^+$, for a finite positive value of Δz. This pattern cannot be interpreted as a transverse mode imposed by the boundaries of the resonator, as the ones of Hermite-Gauss or Laguerre-Gauss families. While the latter self-transform in the Fourier space, the pattern shown in Fig. 2 exhibits non homothetic near field and far field profiles, as commonly observed in large aspect-ratio resonator. The far field profile reveals a bright central spot surrounded by a nearly hexagonal arrangement of weaker spots at 7° with respect the optical axis of the resonator. In the near field we observe an hexagonal pattern with some bright spots. We have analyzed the relationship between the near field profile and each wave-vector component observed in the far field, as shown in Fig. 2 c-f). If we consider only the axial component (central spot in the far field profile), the corresponding near field profile has a Gaussian shape (Fig. 2 d). This component comprises 90% of the optical power of the pattern. If the central spot in the far-field is filtered out, the near field profile obtained has twice the spatial frequency compared to the one obtained without the filter as can be observed in e). This indicates that the near-field profile is determined by the interference between an on-axis plane wave and the hexagonal set of tilted waves which are phase locked. The pattern shown in Fig. 2 is emitted by the VECSEL within a short range of x, for pumping powers 285 mW$<P_p < 400$mW and for a detuning range between the microcavities resonances 4.5 nm$< \delta\lambda < 8$ nm. Within these ranges, the time-averaged profile shown in Fig. 2 is not affected significantly by parameter changes.

The time behavior of the pattern of Fig. 2 is shown in Fig. 3 a). It features multistability between a set of mode-locked states with a number of pulses per roundtrip ranging from zero to five. The corresponding bifurcation diagram of these pulsating solution versus the pump power P_p is explored in Fig. 3 b). Upon increasing the pumping level (P_p), the off solution loses its stability at $P_p = 320$ mW at the advantage of a five-pulses per roundtrip mode-lock state. Then,

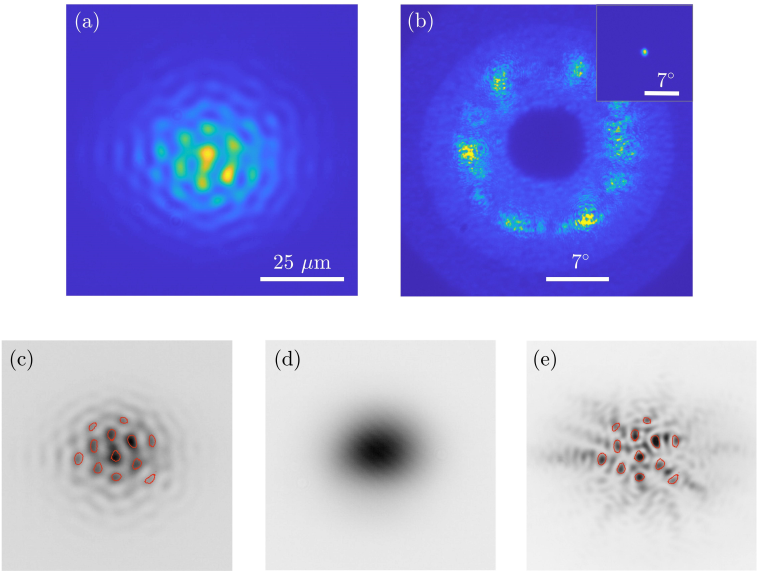

Fig. 2. a) Near field and b) Far field time-averaged profiles of the patterns observed when Δz = +3.3mm and 22μm< x < 27μm. VECSEL is pumped at 320 mW and $\delta\lambda$=5nm. In panel b) the far field has been obtained by filtering out the central part of the profile which carries 90% of the total emitted and hinders the off axis components on the CCD camera. The unfiltered far-field profile is plotted in the inset. This kind of pattern is observed in the range 0.1 mm< Δz < 4 mm. As $| \Delta z | \rightarrow 0$, its existence range in x gets narrower and it requires higher level of pumping. c) Near-field profile with intensity peaks circled in red, d) Near-field profile after filtering out the off-axis Fourier components of the pattern and leaving only the central spot, e) Near-field profile after filtering out the on-axis Fourier components of the pattern (central spot of in the far-field). The contour of the peaks of the total pattern identified in c) are plotted in red.

by decreasing P_p, the VECSEL emission switches to states with a lower number of pulses per roundtrip and, at every jump, P_p is increased to determine the stability of each branch and, when P_p<285 mW, the VECSEL switches to the off solution. The width of the pulse is below the time resolution of our detection system (10 ps, 33 GHz) and auto-correlation measurements of the electromagnetic field gives a coherence time of 2.6 ps which is in agreement with the spectral envelope of 1 nm (267 GHz) FWHM shown Fig. 3 c). Spatially resolved measurements at different points of the pattern reveal that the whole pattern is pulsating as a unique coherent structure.

The multistabilty between different mode-locked states shown in Fig. 3 indicates that the patterns observed are temporal LSs, i.e. they are individually addressable pulses traveling back and forth in the external cavity [27, 30]. In order to demonstrate the possibility of using these pulsating patterns as bits of informations, we have injected a short pump pulse into the gain section to write these temporal localized patterns individually. The system is prepared in the multistable parameter region (285mW< P_p < 318mW) where LSs exist and the amplitude of the addressing pump pulse is chosen to be sufficiently large to bring the system beyond the upper limit of the multistable region, where only the solution composed on five pulses per roundtrip is stable. The addressing pulse is sent to the gain section synchronously with the cavity roundtrip for about

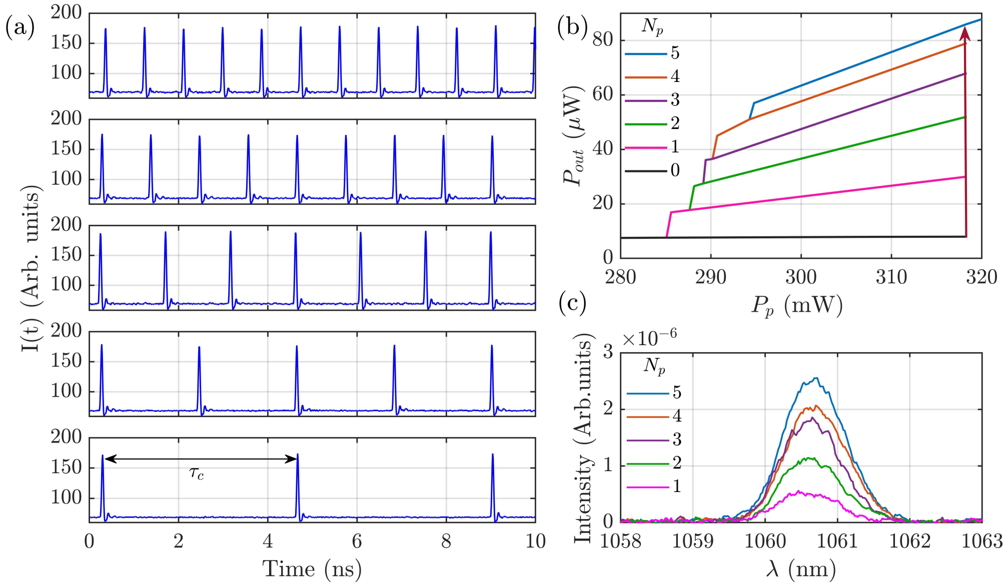

Fig. 3. Spatially integrated intensity output of the pattern shown in Fig. 2. a) Coexisting pulsating states of the pattern, b) Total output power emitted by the VECSEL versus the pump power P_p for different pulsating states of the pattern, ranging from no pulse to five pulses per roundtrip, c) Optical spectra corresponding to different pulsating states of the pattern.

one thousand roundtrips. The addressing process is depicted in Fig. 4 by using a space-time diagram where the pump pulse is represented using a color code, while the trajectory of the LS is represented by a black trace. In Fig. 4 we illustrate the writing operation. In Fig. 4 (left), we choose an initial condition where no LS is present inside the cavity before the addressing pulse. The pump pulse is sufficiently short to switch on a single LS which persists after the perturbation is removed. In Fig. 4 (right) we repeat the operation with a LS already existing in the cavity before the dressing pulse. Other initial conditions can be chosen with similar results, provided that the addressing pulse is separated in time from the preexisting LS of at least τ_g.

4. Discussion and Theoretical Analysis

Our experimental results provide evidence of a novel spatio-temporal laser regime which, to the best of our knowledge, can hardly be traced back to any laser model in the literature. Stationary pattern emission from large aspect-ratio laser has been previously observed and explained as a Turing instability leading to transverse traveling waves [10, 11, 41]. The physical origin of this instability has been attributed to the presence of a (positive) detuning between the gain curve resonance and the closest resonator resonance. The laser emits tilted waves whose frequency matches the gain resonance and whose longitudinal wave vector fulfill the resonance condition of the resonator. This mechanism does not apply to our system where the set of longitudinal cavity resonances is very dense (less than 500 MHz free spectral range) compared to the width of all other relevant spectral filtering curves, such as microcavities resonances (> 9 nm, i.e.more than 1 THz), gain and saturable absorption curves (more than 10 THz).

In order to describe the spatio-temporal dynamics observed we employ the Haus master equation for PML adapted to the long cavity limit [30, 42]. However, this leads to a four

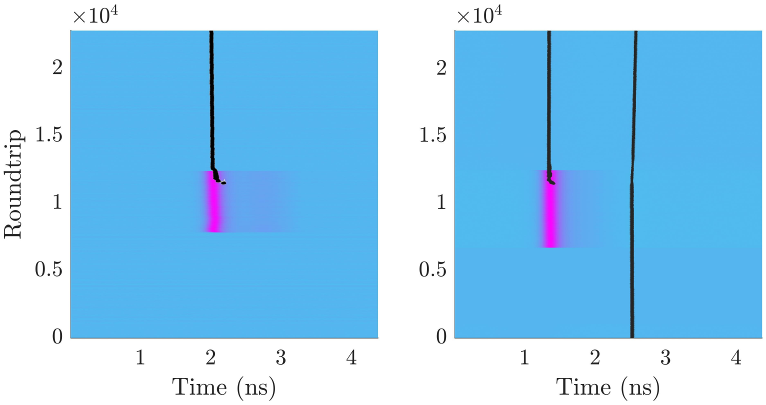

Fig. 4. Spatio-temporal diagram of the writing process of a time localized pattern. The trajectory of the LS is represented by a black trace, while the pump evolution is represented on the space time diagram using a color code is by sending a 120 ps pulse to the gain section between (left) round-trip $n_1 = 7800$ and round-trip $n_2 = 12500$ and (right) between round-trip $n_1 = 6800$ and round-trip $n_2 = 12500$. The pulsed pump beam has a Gaussian spatial profile and a waist of 13 μm

dimensional, stiff, multi-scale partial differential equation (PDE). A qualitative model for the dynamics of the transverse profile of temporal LS, such as the one derived in [43, 44], can be obtained adapting New's method of PML [45] to the situation at hand. This method exploits the scale separation between the pulse evolution, the so-called fast stage in which stimulated emission is dominant, and the slow stage that is controlled by the gain recovery processes. Under the hypothesis that the spatio-temporal profile can be factored into a product of a transverse profile and a short temporal pulse that corresponds to the temporal LS, one can obtain a simplified description of the slow evolution of the transverse profile of the temporal LS $A\left(r_\perp, \theta\right)$ as

$$\frac{\partial A}{\partial \theta} = \left[f\left(|A|^2\right) + \mathcal{L}_\perp\right] A, \tag{4}$$

where θ is the round-trip number and we defined the effective nonlinearity as

$$f\left(P\right) = \left(1 - i\alpha_1\right) J_1\left(r_\perp\right) h\left(P\right) + \left(1 - i\alpha_2\right) J_2 h\left(sP\right) - k, \tag{5}$$

The nonlinear response of the active material to a pulse is $h\left(p\right) = \left(1 - e^{-p}\right)/p$. We define k as the round-trip cavity loss and in Eq. (5) we introduced the line-width enhancement factors α_j of the two active media, that relax toward the pumping power J_j. The ratio of the saturation fluences of the absorber and of the gain is denoted by the parameter s. The effect of finite size optical pumping is taken into account by the spatial dependence of $J_1\left(r_\perp\right) > 0$. Saturable absorption is obtained by setting $J_2 < 0$. It is worth noting that, if the function $h(P)$ is replaced by the Lorentzian line saturation for continuous wave beams $h\left(P\right) \to 1/(1+P)$ in Eqs. (4,5), one obtains the equations obtained in [46, 47], used for describing (stationary) spatial auto-solitons in continuous wave bistable interferometers.

The spatio-temporal linear operator $\mathcal{L}_\perp$ can be determined by using the Fresnel transform [48], which permits the analytical calculation of the transverse effects occurring at each round-trip from the round-trip ABCD matrix. The latter includes diffraction and wavefront curvature occurring in the quasi-telecentric cavity as well as diffraction and thermal lensing (in the parabolic approximation) taking place within the microcavities. In addition, we considered the influence of weak spherical aberrations. The latter are essentially due to the presence of the two short

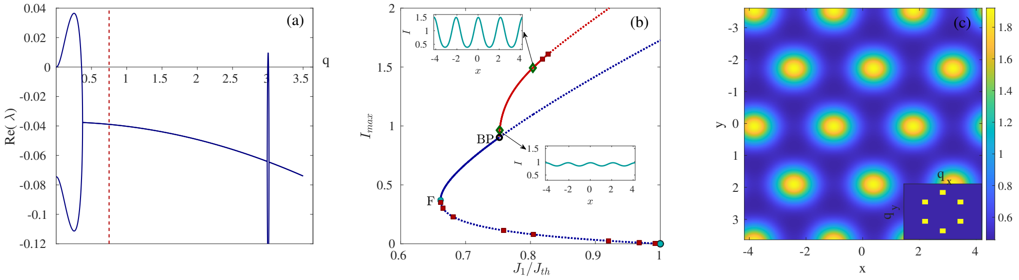

Fig. 5. (a) Stability analysis of the uniform solution over the upper state of the bistable solution branch. A long wavelength modulational instability band is present, however it is inhibited for a system size of $L_\perp = 8.3776$ which corresponds to a low frequency cut-off of $q_c = 2\pi/L_\perp = 0.75$ (orange vertical dashed line). A second narrow band that corresponds to a Turing instability may appear at a wavevector $q_T \simeq \sqrt{\tilde{B}/\tilde{S}} = 3.01$. This diagram is obtained after the emergence of the Turing instability for a value of $J_1 = 0.78 J_{th}$ that corresponds to an intensity $I = 1$. It is above the fold located at $J_F \simeq 0.661 J_{th}$. (b) A branch of CW (blue) and spatially periodic (red) solutions of Eq. (4). The intensity of the field is shown as a function of the scaled gain bias J_1/J_{th}. The stable (unstable) solutions are depicted as solid (dashed) lines. The unstable CW branch bifurcates unstable from the off state and it is stabilized at the fold **F**. The stable periodic branch that corresponds to rolls bifurcates from the CW solution at the branching point BP (black circle) which corresponds to a Turing bifurcation. The emerging pattern further losses its stability via an Andronov-Hopf bifurcation (red square). The two insets show the intensity of the emerging periodic pattern at the points marked as green diamonds. (c) Equivalent regime in two dimensions where we show the intensity profile as well as the far field Fourier spectrum after removal of the on axis homogeneous component (inset). It consists in a regular hexagonal pattern whose wavevector is $|q_T| \simeq 3$ is given by the stability analysis of the uniform state. The bias current is $J_1 = 0.777 J_{th}$ and $\left(L_x, L_y\right) = (8.378, 7.255)$. Other common parameters are: $\widetilde{B} = 1, \widetilde{C} = 0, S = 0.11, \alpha_1 = 1.5,\ \alpha_2 = 0.5,\ J_2 = -0.12,\ k = 0.1,\ s = 15,\ d = 0.003,$

focal distances collimators L_1 and L_4 which are challenged by wide angular spread of the beams. In agreement with experimental observations we assume that $f_c\left(r_\perp\right) = f_0 + \sigma r_\perp^2$ with $\sigma \ll 1$ representing a small aberration coefficient. For the experimental conditions (nearly SI condition and $f_0/f_{2,3} \ll 1$), the effect of spherical aberration can be analytically reduced to a transverse Bilaplacian operator. The details of these calculations will be discussed elsewhere. Describing the wavefront curvature, the diffraction and aberrations as small perturbations to the field profile at each roundtrip, the spatio-temporal linear operator $\mathcal{L}_\perp$ reads

$$\mathcal{L}_\perp = i\widetilde{C}r_\perp^2 + \left(d + i\widetilde{B}\right)\nabla_\perp^2 + i\widetilde{S}\nabla_\perp^4\,, \tag{6}$$

where we define the following dimensionless parameters: the effective diffraction parameter $\tilde{B} = \lambda B_{RT}/(4\pi) + l_{1,\perp}^2 + l_{2,\perp}^2$, the wavefront curvature $\tilde{C} = \pi C_{RT}/\lambda$ and the aberration parameter $\tilde{S} = \left(\frac{\lambda}{2\pi}\right)^3 \sigma f_0^2$. Here, B_{RT} and C_{RT} are, respectively, the coefficients B and C of the ray transfer roundtrip matrix and $l_{j,\perp}$ being the normalized micro-cavity diffraction lengths. As shown in Eq. (3) (see also Supplemental 1-2C), close to self-imaging conditions, $B_{RT} \approx 2(M^2\Delta x)$ and $C_{RT} \approx -2\frac{\Delta z}{f_c^2}$, hence Δx controls the diffraction while Δz rules the wavefront curvature which is equivalent to a parabolic transverse potential in Eq. (6. The finite size of lenses and the numerical aperture of the whole optical system is modeled by a diffusion parameter d that penalizes high transverse spatial frequencies $q_\perp$.

Close to SI condition, for positive diffraction ($\Delta x \gtrsim 0$), the VECSEL resonator is stable for focusing wavefront curvature ($\tilde{C} \lessapprox 0$, i.e. $\Delta z \gtrapprox 0$). Experimental results show that, when $\widetilde{B} \rightarrow 0$, a modulated pattern featuring well defined transverse wave vectors appear. This phenomenology can be explained as the result of a supercritical Turing instability. It was shown in [49] that Eq. (4) forbids the appearance of a Turing instability while it allows for a long wavelength instability and the formation of a band of unstable spatial frequencies in the range $q \in [0, q_M]$. However, the presence of the Bilaplacian operator describing optical aberrations changes this picture, as it introduces a new spatial scale in the system and it renders the appearance of a Turing bifurcation possible. This is shown in Fig. 5(a) where we plot the result of the stability analysis of the homogeneous state for a value of the pump within the bistability region where the VECSEL emits temporal LS. The real part of the two dominant eigenvalues reveals the presence of a Turing instability at a wave-vector $q_T \simeq \sqrt{\widetilde{B}/\widetilde{S}}$ in addition to the band of unstable spatial frequencies in the range $q \in [0, q_M]$. It is worth noting that the finite size of the pump profile imposes a low frequency cut-off for the wave-vectors allowed in the system, $q_c = 2\pi/L_\perp$. This spatial frequency filtering eventually controls which instability can develop : if $q_M < q_c$ the long wavelength instability is inhibited and the Turing pattern remains the unique spatial instability that can emerge, provided that q_T is resonant, i.e. an integer multiple of q_c, i.e with $n \in \mathbb{N}$. Consequently, this instability can be expected to appear by tuning the value of $\widetilde{B}$ within narrow range, in good agreement with experimental observations.

In Fig. 5(b) we show the result of numerical simulations of Eq. (4) as well as path continuation using Pde2Path [50] for a system with one transverse spatial dimension and with homogeneous pumping. It reveals that a homogeneous emission of temporal LS appear subcritically below the lasing threshold. The corresponding C-shape is represented by the blue line in Fig. 5(b). When the system size is chosen such that $q_T/q_c = 4$, a periodic pattern can emerge from a homogeneous emission while increasing the pump power. As in the experiment, the periodic pattern appears as a modulation of an homogeneous on-axis emission which dominates the far-field profile. This Turing pattern can be observed at a fixed pump level by tuning the value $\widetilde{B}$, as this parameter will change the value of the critical wave-vector q_T with respect to $4q_c$. In this case the pattern will appear with a finite modulation amplitude of the homogeneous emission, fixed by the pump power. In two transverse dimensions, the dynamics is more complex since only the magnitude of the unstable wave-vector $|q_T|$ is fixed by the linear stability analysis leading to an annular distribution of unstable wave vectors in the two-dimensional plane spanned by $q_\perp = (q_x, q_y)$. Stripes, squares or hexagonal patterns can be selected depending on the kind of nonlinearity coupling the different wave-vectors that must all emerge with magnitude $|q_T|$. However, the structure of the nonlinearity in Eq. 4 favors the emergence of hexagonal patterns as can be seen in Fig. 5(c). The far field represented in the inset of Fig. 5(c) exhibits (in Log scale) the typical spectrum associated with hexagonal patterns after filtering out the on-axis component. The value of $q_T \sim 3$ matches the result of the linear stability analysis.

In conclusion, we have realized and operated a laser platform enabling the investigation of fully developed spatio-temporal dynamics. In this paper, we have operated it in the regime of spatio-temporal mode-locking and we have reported the first observation of temporal localized Turing patterns, but other novel laser regimes will be investigated in the future, including the generation of spatio-temporal LS, also called dissipative light bullets [43]. The theoretical analysis has revealed the important role of optical aberrations when approaching SI condition, thus suggesting that spatial control of light in our VECSEL will demand aberration engineered optical elements and/or counterbalancing nonlinear effects. An alternative path is based on the introduction of spatially patterned laser parameters. In particular, the spatial shaping of the pumped region opens interesting perspectives since, thanks to SI condition, the pump pattern will be reproduced in the near-field emission of the laser. This can be achieved, for example, by depositing an absorptive mask onto the gain mirror. Preliminary results indicate the possibility of implementing spatially decorrelated sources of temporal LS in a single VECSEL.

As illustrated in [36], several applications can be envisaged for the VECSEL we have studied in this paper. Among them we underline spatio-temporal processing of information, frequency combs multiplexing in the same cavity [51] and speckle-free imaging with short pulses [52].

Funding. The INPHYNI Group acknowledges project ANR-18-CE24-0002 BLASON and funding of Région PACA OPTIMAL. J.J. acknowledges financial support from project MOVELIGHT (PGC2018-099637-B-100 AEI/FEDER UE).

Supplemental document. See Supplement 1 for supporting content.

References

1. F. Arecchi, S. Boccaletti, and P. Ramazza, "Pattern formation and competition in nonlinear optics," Phys. Reports **318**, 1–83 (1999).
2. L. Lugiato, "Transverse nonlinear optics: Introduction and review," Chaos, Solitons Fractals **4**, 1251–1258 (1994). Special Issue: Nonlinear Optical Structures, Patterns, Chaos.
3. P. Coullet, L. Gil, and F. Rocca, "Optical vortices," Opt. Commun. **73**, 403–408 (1989).
4. G.-L. Oppo, G. D'Alessandro, and W. J. Firth, "Spatiotemporal instabilities of lasers in models reduced via center manifold techniques," Phys. Rev. A **44**, 4712–4720 (1991).
5. K. Staliunas, "Laser ginzburg-landau equation and laser hydrodynamics," Phys. Rev. A **48**, 1573–1581 (1993).
6. G. Huyet, M. C. Martinoni, J. R. Tredicce, and S. Rica, "Spatiotemporal dynamics of lasers with a large fresnel number," Phys. Rev. Lett. **75**, 4027–4030 (1995).
7. J. Lega, J. Moloney, and A. Newell, "Swift-hohenberg equation for lasers," Phys. Rev. Lett. **73**, 2978–2981 (1994).
8. P. K. Jakobsen, J. Lega, Q. Feng, M. Staley, J. V. Moloney, and A. C. Newell, "Nonlinear transverse modes of large-aspect-ratio homogeneously broadened lasers: I. analysis and numerical simulation," Phys. Rev. A **49**, 4189–4200 (1994).
9. F. T. Arecchi, G. Giacomelli, P. L. Ramazza, and S. Residori, "Vortices and defect statistics in two-dimensional optical chaos," Phys. Rev. Lett. **67**, 3749–3752 (1991).
10. K. Staliunas, G. Slekys, and C. O. Weiss, "Nonlinear pattern formation in active optical systems: Shocks, domains of tilted waves, and cross-roll patterns," Phys. Rev. Lett. **79**, 2658–2661 (1997).
11. S. P. Hegarty, G. Huyet, J. G. McInerney, and K. D. Choquette, "Pattern formation in the transverse section of a laser with a large fresnel number," Phys. Rev. Lett. **82**, 1434–1437 (1999).
12. V. B. Taranenko, K. Staliunas, and C. O. Weiss, "Spatial soliton laser: Localized structures in a laser with a saturable absorber in a self-imaging resonator," Phys. Rev. A **56**, 1582–1591 (1997).
13. Y. Tanguy, T. Ackemann, W. J. Firth, and R. Jäger, "Realization of a semiconductor-based cavity soliton laser," Phys. Rev. Lett. **100**, 013907 (2008).
14. P. Genevet, S. Barland, M. Giudici, and J. R. Tredicce, "Cavity soliton laser based on mutually coupled semiconductor microresonators," Phys. Rev. Lett. **101**, 123905 (2008).
15. T. Elsass, K. Gauthron, G. Beaudoin, I. Sagnes, R. Kuszelewicz, and S. Barbay, "Fast manipulation of laser localized structures in a monolithic vertical cavity with saturable absorber," Appl. Phys. B **98**, 327–331 (2010).
16. P. Genevet, S. Barland, M. Giudici, and J. R. Tredicce, "Bistable and addressable localized vortices in semiconductor lasers," Phys. Rev. Lett. **104**, 223902 (2010).
17. P. Coullet, C. Riera, and C. Tresser, "A new approach to data storage using localized structures," Chaos **14**, 193–201 (2004).
18. M. Tlidi, P. Mandel, and R. Lefever, "Localized structures and localized patterns in optical bistability," Phys. Rev. Lett. **73**, 640–643 (1994).
19. N. N. Rosanov and G. V. Khodova, "Autosolitons in bistable interferometers," Opt. Spectrosc. **65**, 449 (1988).
20. M. Brambilla, L. A. Lugiato, F. Prati, L. Spinelli, and W. J. Firth, "Spatial soliton pixels in semiconductor devices," Phys. Rev. Lett. **79**, 2042–2045 (1997).
21. L. Lugiato, "Introduction to the feature section on cavity solitons: An overview," Quantum Electron. IEEE J. **39**, 193–196 (2003).
22. S. Barland, J. R. Tredicce, M. Brambilla, L. A. Lugiato, S. Balle, M. Giudici, T. Maggipinto, L. Spinelli, G. Tissoni, T. Knödl, M. Miller, and R. Jäger, "Cavity solitons as pixels in semiconductor microcavities," Nature **419**, 699–702 (2002).
23. F. Leo, S. Coen, P. Kockaert, S. Gorza, P. Emplit, and M. Haelterman, "Temporal cavity solitons in one-dimensional kerr media as bits in an all-optical buffer," Nat Photon **4**, 471–476 (2010).
24. T. Herr, V. Brasch, J. D. Jost, C. Y. Wang, N. M. Kondratiev, M. L. Gorodetsky, and T. J. Kippenberg, "Temporal solitons in optical microresonators," Nat. Photonics **8**, 145–152 (2014).
25. A. Bao, Hualongand Cooper, M. Rowley, L. Di Lauro, J. S. Totero Gongora, S. T. Chu, B. E. Little, G.-L. Oppo, R. Morandotti, D. J. Moss, B. Wetzel, M. Peccianti, and A. Pasquazi, "Observation of mode-locked spatial laser solitons," Nat. Photonics. **13**, 384–389 (2019).
26. N. Englebert, C. Mas-Arabi, P. Parra-Rivas, S. Gorza, and F. Leo, "Temporal solitons in a coherently driven active resonator," Nat. Photonics. **15**, 536–541 (2021).

27. M. Marconi, J. Javaloyes, S. Balle, and M. Giudici, “How lasing localized structures evolve out of passive mode locking,” Phys. Rev. Lett. **112**, 223901 (2014).
28. M. Marconi, J. Javaloyes, P. Camelin, D. Gonzalez, S. Balle, and M. Giudici, “Control and generation of localized pulses in passively mode-locked semiconductor lasers,” Sel. Top. Quantum Electron. IEEE J. **21**, 1–10 (2015).
29. M. Marconi, J. Javaloyes, P. Camelin, D. Chaparro, S. Balle, and M. Giudici, “Control and generation of localized pulses in passively mode-locked semiconductor lasers,” Sel. Top. Quantum Electron. IEEE J. **PP**, 1–1 (2015).
30. P. Camelin, J. Javaloyes, M. Marconi, and M. Giudici, “Electrical addressing and temporal tweezing of localized pulses in passively-mode-locked semiconductor lasers,” Phys. Rev. A **94**, 063854 (2016).
31. P. Camelin, C. Schelte, A. Verschelde, A. Garnache, G. Beaudoin, I. Sagnes, G. Huyet, J. Javaloyes, S. Gurevich, and M. Giudici, “Temporal localized structures in mode-locked vertical external-cavity surface-emitting laser,” Opt. Lett. **43**, 5367 (2018).
32. F. Encinas-Sanz, S. Melle, and O. G. Calderón, “Time-resolved dynamics of two-dimensional transverse patterns in broad area lasers,” Phys. Rev. Lett. **93**, 213904 (2004).
33. F. Gustave, N. Radwell, C. McIntyre, J. P. Toomey, D. M. Kane, S. Barland, W. J. Firth, G.-L. Oppo, and T. Ackemann, “Observation of mode-locked spatial laser solitons,” Phys. Rev. Lett. **118**, 044102 (2017).
34. L. G. Wright, D. N. Christodoulides, and F. W. Wise, “Spatiotemporal mode-locking in multimode fiber lasers,” Science **358**, 94–97 (2017).
35. L. G. Wright, P. Sidorenko, H. Pourbeyram, Z. M. Ziegler, A. Isichenko, B. A. Malomed, C. R. Menyuk, D. N. Christodoulides, and F. W. Wise, “Mechanisms of spatiotemporal mode-locking,” Nat. Phys. **16**, 565–270 (2020).
36. L. G. Wright, W. H. Renninger, D. N. Christodoulides, and F. W. Wise, “Nonlinear multimode photonics: nonlinear optics with many degrees of freedom,” Optica **9**, 824–841 (2022).
37. Y. Noblet and T. Ackemann, “Analysis of spatial emission structures in vertical-cavity surface-emitting lasers with feedback from a volume bragg grating,” Phys. Rev. A **85**, 053812 (2012).
38. C. Schelte, J. Javaloyes, and S. V. Gurevich, “Dynamics of temporally localized states in passively mode-locked semiconductor lasers,” Phys. Rev. A **97**, 053820 (2018).
39. A. Laurain, M. Myara, G. Beaudoin, I. Sagnes, and A. Garnache, “High power single–frequency continuously–tunable compact extended–cavity semiconductor laser,” Opt. Express **17**, 9503–9508 (2009).
40. A. Garnache, S. Hoogland, A. Tropper, I. Sagnes, G. Saint-Girons, and J. S. Roberts, “Sub-500-fs soliton-like pulse in a passively mode-locked broadband surface-emitting laser with 100 mW average power,” Appl. Phys. Lett. **80**, 3892–3894 (2002).
41. Q. Feng, J. V. Moloney, and A. C. Newell, “Amplitude instabilities of transverse traveling waves in lasers,” Phys. Rev. Lett. **71**, 1705–1708 (1993).
42. J. Hausen, K. Lüdge, S. V. Gurevich, and J. Javaloyes, “How carrier memory enters the haus master equation of mode-locking,” Opt. Lett. **45**, 6210–6213 (2020).
43. J. Javaloyes, “Cavity light bullets in passively mode-locked semiconductor lasers,” Phys. Rev. Lett. **116**, 043901 (2016).
44. S. V. Gurevich and J. Javaloyes, “Spatial instabilities of light bullets in passively-mode-locked lasers,” Phys. Rev. A **96**, 023821 (2017).
45. G. New, “Pulse evolution in mode-locked quasi-continuous lasers,” Quantum Electron. IEEE J. **10**, 115 – 124 (1974).
46. N. N. Rosanov and G. V. Khodova, “Autosolitons in nonlinear interferometers,” Opt. Spectrosc. **65**, 449–450 (1988).
47. A. G. Vladimirov, S. V. Fedorov, N. A. Kaliteevskii, G. V. Khodova, and N. N. Rosanov, “Numerical investigation of laser localized structures,” J. Opt. B: Quantum Semiclassical Opt. **1**, 101 (1999).
48. C. Palma and V. Bagini, “Extension of the fresnel transform to abcd systems,” J. Opt. Soc. Am. A **14**, 1774–1779 (1997).
49. S. V. Fedorov, A. G. Vladimirov, G. V. Khodova, and N. N. Rosanov, “Effect of frequency detunings and finite relaxation rates on laser localized structures,” Phys. Rev. E **61**, 5814–5824 (2000).
50. H. Uecker, D. Wetzel, and J. D. M. Rademacher, “pde2path - a matlab package for continuation and bifurcation in 2d elliptic systems,” Numer. Math. Theory, Methods Appl. **7**, 58–106 (2014).
51. J. Pupeikis, B. Willenberg, S. L. Camenzind, A. Benayad, P. Camy, C. R. Phillips, and U. Keller, “Spatially multiplexed single-cavity dual-comb laser,” Optica **9**, 713–716 (2022).
52. S. Knitter, C. Liu, B. Redding, M. K. Khokha, M. A. Choma, and H. Cao, “Coherence switching of a degenerate vecsel for multimodality imaging,” Optica **3**, 403–406 (2016).

Supplementary Files

- supplementalsubmitted.pdf